Interannual variability of isotopic composition in water vapor over West Africa and its relation to ENSO

By

Atsushi Okazaki[1], Yusuke Satoh[1], Guillaume Tremoy[2], Françoise Vimeux[2, 3], Remco Scheepmaker[4], and Kei Yoshimura[1, 5]

[1]Institute of Industrial Science, University of Tokyo, Tokyo, Japan
[2]Laboratoire des Sciences du Climat et de l'Environnement, UMR8212, Institut Pierre Simon Laplace, CEA-CNRS-UVSQ, Gif-sur-Yvette, France
[3]Laboratoire HydroSciences Montpellier, UMR 5569, Institut de Recherche pour le Développement, CNRS-IRD-UM1-UM2, Montpellier, France
[4]SRON Netherlands Institute for Space Research, Utrecht, The Netherlands
[5]Atmosphere and Ocean Research Institute, University of Tokyo, Kashiwa, Japan

Submitted to Atmospheric Chemistry and Physics Discussions
Submitted on May 2014
Revised on Sep 2014
Revised on Jan 2015

Corresponding author: Atsushi Okazaki, Institute of Industrial Science, University of Tokyo, 4-6-1 Meguro, Komaba, Tokyo, 153-8505, Japan. (okazaki@rainbow.iis.u-tokyo.ac.jp)

Abstract

This study was performed to examine the relationship between isotopic composition in near-surface vapor ($\delta^{18}O_v$) over West Africa during the monsoon season and El Niño-Southern Oscillation (ENSO) activity using the Isotope-incorporated Global Spectral Model. The model was evaluated using a satellite and in situ observations at daily to interannual timescales. The model provided an accurate simulation of the spatial pattern and seasonal and interannual variations of isotopic composition in column and surface vapor and precipitation over West Africa. Encouraged by this result, a simulation stretching 34 years (1979 – 2012) was conducted to investigate the relation between atmospheric environment and isotopic signature at the interannual time scale. The simulation indicated that the depletion in the monsoon season does not appear every year at Niamey. The major difference between the composite fields with and without depletion was in the amount of precipitation in the upstream area of Niamey. As the interannual variation of the precipitation amount is influenced by the ENSO, we regressed the monsoon season averaged $\delta^{18}O_v$ from the model and annually averaged NINO3 index, and found a statistically significant correlation (R = 0.56, $P < 0.01$) at Niamey. This relation suggests that there is a possibility of reconstructing past West African monsoon activity and ENSO using

climate proxies.

1. Introduction

The El Niño-Southern Oscillation (ENSO) is the strongest mode of interannual variability in the tropics (Dai et al., 1997) and plays an important role in variability of precipitation, temperature, and circulation patterns on this timescale. El Niño can cause catastrophic floods and droughts (Philander, 1983) and damage to ecosystems (Aronson et al., 2000). A recent study projected an increase in the frequency of extreme El Niño events due to global warming (Cai et al., 2014). Therefore, it is essential to understand the natural variability of ENSO. Stable water isotopes (D, ^{18}O) have been used to infer past and present climate since the work of Dansgaard (1964). Several studies have linked ENSO with isotopic variation in precipitation or in seawater under the present climate (e.g., Schmidt et al., 2007; Yoshimura et al., 2008; Tindall et al., 2009). For example, tropical South America (Vuille and Werner, 2005), Western and Central Pacific (Brown et al., 2006), and the Asian monsoon region (Ishizaki et al., 2012) are identified as having a connection with ENSO, basically through changes in local rainfall or integrated rainfall along the trajectory. However, other regions, such as West Africa, have not yet been investigated in detail.

West Africa receives most precipitation in the monsoon season (July – September; JAS) and is known for its high variability at interannual or longer timescales. The severe drought that hit West Africa during the 1970s and 1980s prompted researchers to study the factors controlling West African rainfall variability at interannual to multidecadal timescales (e.g., Folland et al., 1986; Palmer, 1986; Janicot et al., 1996; Giannni et al., 2003; Shanahan et al., 2009; Mohino et al., 2011a, b). At present, the major role of sea surface temperatures (SST) in driving the variability with land–atmosphere interactions as an amplifier (Giannni et al., 2003) is widely recognized. However, there is still debate regarding the relative importance of the various basins and mechanistic timescales involved (Nicholson, 2013). The Atlantic (Lamb, 1978; Joly and Voldoire, 2010; Mohino et al., 2011a), Pacific (Janicot et al., 2001; Mohino et al., 2011b), Indian Ocean (Palmer et al., 1986), and Mediterranean (Rowell, 2003; Polo et al., 2008) are all candidates. Among them, the ENSO is thought to modulate the high-frequency component (interannual) of the variability (Ward, 1998; Joly et al., 2007). However, the relationships are not stationary over time; the West African rainfall is correlated with ENSO only after the 1970s (Janicot et al., 2001; Losada et al., 2012), indicating the existence of multiple competing physical mechanisms. How the impact has changed remains an open question.

Several studies used isotopes to understand the water cycle over West Africa at the intraseasonal timescale. Risi et al. (2008b) and Tremoy et al. (2012; 2014) examined the isotopic compositions of precipitation ($\delta^{18}O_P$) and vapor ($\delta^{18}O_v$), respectively, and both found that $\delta^{18}O$ records the spatially and temporally integrated convective activity during the monsoon season. Here δ in per mil units is defined as $(R_{sample}/R_{std}-1) \times 1000$, where R_{std} is VSMOW: Vienna Standard Mean Ocean Water. Risi et al. (2010) confirmed the relation using the LMDZ-iso model and suggested that $\delta^{18}O$ is controlled by convection through rain re-evaporation and the progressive depletion of the vapor by convective mixing along air mass trajectories. The relation between $\delta^{18}O$ and convective activity suggests the possibility of reconstructing the convective activity using a climate proxy, if the relation holds at the interannual timescale. The long record of precipitation should help in determining how SSTs influence precipitation variability. Some studies reconstructed precipitation over West Africa (Lézine and Casanova, 1989; Shanahan et al., 2009). Shanahan et al. (2009) directly tied isotopic composition with the local precipitation. However it is possible that the amount of rainfall along the trajectory has more impact rather than local information, as mentioned above. Therefore it is still necessary to estimate the relative contributions of the main controls on interannual variability of the isotopic composition in more comprehensive way.

In this paper, we explore the factors governing the interannual variability of monsoon season $\delta^{18}O_v$, which is the source of precipitation and controls $\delta^{18}O_p$ variability (Risi et al., 2008a), over West Africa and how the ENSO signal is imprinted. As the observations cover relatively short periods to look into the interannual variability and available variables are limited, we use an isotope-enabled general circulation model (GCM) to complement the observations.

In the following section, the model simulations and the observations are described. In Sect. 3, we compare the simulated and observed variability of $\delta^{18}O$ at daily to interannual timescale. Section 4 investigates the factors controlling $\delta^{18}O_v$ at the interannual timescale by analyzing the simulation results and confirms the role of the identified factors by sensitivity experiments. Finally, we examine the relation between $\delta^{18}O$ and ENSO in Sect. 5.

2. Data and methods

2.1. Observations

2.1.1. Observation of HDO in vapor from space

Frankenberg et al. (2009) measured column-averaged isotopologue ratio (δD) values in water vapor using the SCanning Imaging Absorption spectroMeter for Atmospheric CHartographY (SCIAMACHY) onboard the European research satellite ENVISAT. We used the updated and extended version of this dataset from Scheepmaker et al. (2014), covering the years 2003 – 2007. As measured δD is weighted by the H_2O concentration at all heights, it is largely determined by the isotopic abundance in the lowest tropospheric layers, where most water vapor resides. The footprint of each measurement is 120 km (across-track) × 30 km (along-track). We apply the following selection criteria concerning the retrievals (Scheepmaker et al., 2014):

- Retrieved H_2O total column must be at least 70% of the a priori value.
- The CH_4 column in the same retrieval window must be at least within 10% of the a priori value.
- Root-mean-square variation of the spectral residuals must be below 5%.
- Convergence achieved in a maximum of four iteration steps.

Here, the first two criteria restrict large deviations from the a priori H_2O and CH_4 columns, which are normally the result of light scattering by clouds. Therefore, these two criteria function as a simple cloud filter. Due to high detector noise of SCIAMACHY in the short-wave infrared channels, the single measurement noise (1-sigma) is typically 40‰ – 100‰, depending on total water column, surface albedo, and viewing geometry. For the region of our study, however, the mean single measurement noise is of the order of 20‰ – 50‰, due to the high albedo and optimal viewing geometry of West Africa. This random error can be further reduced by averaging multiple measurements. Therefore, we average the measurements according to the procedure of Yoshimura et al. (2011); we averaged multiple measurements that were collected in a grid of 2.5° × 2.5° in 6 h. We set the threshold value for averaging to 10, meaning that the average of the SCIAMACHY measurements in every grid cell is based on at least 10 measurements taken within 6 h. From the IsoGSM simulation results, the times of the nearest satellite measurements were extracted (hereafter the process is called “collocation”). Thus, there was no difference in representativeness between the model and the satellite data.

2.1.2. In situ measurement of water isotopologues in vapor

To assess the performance of the model at shorter timescales, daily $\delta^{18}O_v$ from Tremoy et al. (2012) was used in this study. The $\delta^{18}O_v$ was observed at about 8 m above the ground using a Picarro laser instrument (L1102-i model) with an accuracy of ± 0.25‰ at the Institut des Radio-Isotopes in Niamey, Niger (IRI, 13.31°N 2.06°E, 218 m.a.s.l) from 2 July 2010 to 12 May 2011.

2.1.3. In situ measurement of isotopes in precipitation (GNIP)

Observations of the monthly isotope ratio in precipitation over West Africa were obtained from the Global Network for Isotopes in Precipitation (GNIP) observational database (IAEA/WMO, 2014). We chose 28 GNIP stations in Africa that have full annual data spanning more than 10 years. The observatory location and its operation period are summarized in Table 1.

2.2. Isotope-enabled General Circulation Model simulation

The Isotope-incorporated Global Spectral Model (IsoGSM) is an atmospheric GCM, into which stable water isotopes are incorporated. The model uses T62 horizontal resolution (about 200 km) and 28 vertical levels, and temporal resolution of the output is 6h. The convection scheme is the Relaxed Arakawa-Schubert Scheme (Moorthi and Suarez, 1992). The main time integration scheme is leapfrog scheme. The model is spectrally nudged toward wind and temperature fields from the National Centers for Environmental Prediction (NCEP)/Department of Energy (DOE) Reanalysis 2 (R2) (Kanamitsu et al., 2002) in addition to being forced with prescribed SST and sea ice from NCEP analysis, which are the same as the one used in NCEP/DOE R2 (Kanamitsu et al., 2002). After a spin-up period of about 10 years with the constant 1979 forcing, the simulation was run from 1979 to 2012 as in Yoshimura et al. (2008). Isotope processes were incorporated following Joussaume et al. (1984): Isotopic fractionation takes place whenever phase transition occurs. Most fractionation can be assumed to occur at thermodynamic equilibrium, except for three particular cases; surface evaporation form open water; condensation from vapor to ice in supersaturation conditions under -20 deg-C; and evaporation and isotopic exchange from liquid raindrop into unsaturated air. IsoGSM assumes no fractionation when water evapotranspires over land. More details of the model configurations were described previously (Yoshimura et al., 2008). The general reproducibility of the model for daily to interannual time scales is well evaluated by comparing with precipitation isotope ratio (Yoshimura et al., 2008) and vapor isotopologue ratio from satellite measurements (Yoshimura et al., 2011), and showed sufficiently accurate results for various process studies (e.g., Berkelhammer et al., 2012; Liu et al., 2013; Liu et al., 2014).

In addition to the standard experiment (Std) mentioned above, we carried out two sensitivity experiments. The first of these experiments examined the sensitivity of the results to the "equilibrium fraction ε," which is the degree to which falling rain droplets equilibrate with the surroundings. Risi et al. (2010) reported the importance of re-evaporation for $\delta^{18}O_v$ over West Africa, and Yoshimura et al. (2011) found an improved simulation result with the changed parameter. Following Yoshimura et al. (2011), we set this value to 10%, while in the standard simulation it was set to 45%. The other sensitivity experiment was to estimate the contributions to interannual variability in $\delta^{18}O_v$ of the distillation effect during transportation from the source regions. In this experiment, we removed the influences of the distillation processes by turning off isotopic fractionation during condensation and re-evaporation from raindrops and preventing isotopic exchange between falling raindrops and the surrounding vapor. Note that these effects were switched off only in a certain region in the simulation. For a similar purpose, Ishizaki et al. (2012) specified transport pathways and then removed these effects along the pathway. We chose a different means of removing the effects in a certain domain, as we wished to specify the area that plays an important role in controlling the isotopic variation at a point. Hereafter, we refer to the former sensitivity experiment as the "E10" experiment and the latter as the "NoFrac" experiment. Std and NoFrac cover the 1979 – 2012 period, and E10 covers the 2010 – 2011 period. The simulation results used in this study are basically from Std unless otherwise noted.

We use both δD and $\delta^{18}O$ in the evaluation of the model, since SCIAMACHY observes δD whereas Tremoy et al. (2012) observes $\delta^{18}O$. As δD and $\delta^{18}O$ basically respond to meteorological factors in the same way, there are no differences in underlying mechanisms to produce changes. Therefore, there is no problem using the combination of δD and $\delta^{18}O$ to evaluate model performance. In the other section we consistently use $\delta^{18}O$.

2.3. Isoflux analysis

Isoflux analysis specifies the contributions of advection, evapotranspiration, and precipitation to the changes in the isotopic composition of precipitable water in an atmospheric column. The concept of the analysis is based on budget analysis. Using such analysis, Lai et al. (2006) specifies the factors controlling $\delta^{18}O_v$ in a canopy layer. Worden et al. (2007) found the importance of re-evaporation from raindrops. Here, we developed the mass balance equation for ^{18}O in the atmospheric column. The mass balance for total precipitable water inside the atmospheric column can be written as:

$$\frac{dW}{dt} = -\nabla \cdot Q + E - P \qquad (1)$$

where W represents the total precipitable water, Q is the vertically integrated two-dimensional vapor flux vector, E is evapotranspiration, and P is precipitation. The term $\nabla \cdot Q$ denotes the horizontal divergence of vapor flux. Here, we refer to this term as advection. A mass balance equation can also be written for ^{18}O in the same manner as Eq. (1).

$$\frac{dR_W W}{dt} = -\nabla \cdot R_W Q + R_E E - R_P P \qquad (2)$$

where R_W, R_E, and R_P represent the isotope ratio ($^{18}O/^{16}O$) of precipitable water, evapotranspiration, and precipitation, respectively. Multiplying Eq. (1) by R_W, and subtracting that from Eq. (2) we obtain:

$$\frac{dR_W}{dt}W = -\nabla R_W \cdot Q + (R_E - R_W)E - (R_P - R_W)P \, . \quad (3)$$

Dividing by the R_{std}, we can rewrite Eq. (3) in δ notation as:

$$\frac{d\delta_W}{dt}W = -\nabla \delta_W \cdot Q + (\delta_E - \delta_W)E - (\delta_P - \delta_W)P \, . \quad (4)$$

Starting from the left, the terms represent the temporal derivative of the isotopic composition of precipitable water, the effect of advection, evapotranspiration, and precipitation to deplete or enrich the precipitable water, respectively. As the analysis specifies the contribution of each factor to the change in isotopic composition of precipitable water, the analysis period should start before initiation of isotopic depletion and end at the most depleted point. We use the 6h output of IsoGSM to calculate each term in Eq. (4), then each term is averaged over the targeting period and compared.

3. Evaluation of IsoGSM

3.1. Evaluation of IsoGSM at the mean state and seasonal climatology

The annual mean climatology of the SCIAMACHY data and the collocated IsoGSM fields together with precipitable water by JRA25 (Onogi et al., 2007) and the model are shown in Fig. 1. In the SCIAMACHY data, the meridional gradient over West Africa is notable; the lowest values of δD were found in the Sahara and the highest in the Guinea coast. This is due to the dry and therefore HDO-depleted air mass from the subsiding branch of the Hadley circulation in the dry season over the Sahara and strong evaporation and/or recycling of water in the Tropics (Frankenberg et al., 2009). IsoGSM simulates this spatial pattern qualitatively well. Although the average is negatively biased (about 20‰) (Yoshimura et al., 2011) and the latitudinal gradient is weaker in IsoGSM, bias and overestimated gradient is found in SCIAMACHY when compared with ground-based Fourier-Transform Spectrometers (Scheepmaker et al., 2014). Accordingly we cannot conclude such differences from the satellite is indeed problematic or not at this stage.

Figure 2 shows time–latitude diagrams of δD and precipitable water averaged on 5°W – 5°E from 2003 to 2007. Over the region, vapor δD is high and wet in the monsoon season and low in the dry season. In the monsoon season, the wet and isotopically heavy vapor comes from the south along with the monsoon flow. The northern end of the flow coincides with the location of the Inter-Tropical Discontinuity (ITD), which limits the extension of the monsoon flow (Janicot et al., 2008). In the dry season, the subsiding branch of the Hadley cell brings a dry and depleted air mass to the north of the area (Frankenberg et al., 2009). Around 10°N, δD has two minima; one in winter reflecting the depleting effect of subsidence, and the other in summer reflecting the depleting effect of convective activity (Risi et al., 2010). The model captures these two regimes and the depleting effect of convective activity around 10°N in the monsoon season. Pearson product moment correlation coefficient (hereafter we use the term “correlation” unless otherwise noted) between the observed and simulated zonally averaged δD (5°W-5°E) is 0.77 (significance level: $P < 0.001$). Note that the range is widely different between them (–300‰ – 0‰ for SCIAMACHY; –190‰ – 90‰ for IsoGSM). This may be because IsoGSM misses the enrichment in boreal summer over tropical Africa, as suggested in previous studies (Frankenberg et al., 2009; Yoshimura et al., 2011). The bias in the mean field (Risi et al., 2010; Werner et al., 2011; Lee et al., 2012) and the underestimated seasonality (Risi et al., 2010) are also common in other GCMs. Again, the bias in SCIAMACHY has been indicated as well (Scheepmaker et al., 2014), and Risi et al. (2010) pointed out the possibility that SCIAMACHY may overestimate the variability by preferentially sampling high altitudes.

Then we compared the simulated $\delta^{18}O_v$ with in situ measurement from Tremoy et al. (2012)

in Niamey grid point over the 2010 – 2011 period. Figure 3 shows the time series of near surface daily $\delta^{18}O_v$ from the observation and IsoGSM, and the statistics are summarized in Table 2. Note that only the days for which observations were available were used to calculate the statistics. These measurements also showed the two isotopic minima of the year (W-shape); the first in August and September, and the second in January associated with the convective activity and large scale subsidence respectively. The model nicely captures the two minima and simulates well the average and variability, especially in the dry season. On the other hand, the model reveals rather poor reproducibility of day-to-day variation during the monsoon season; the depletion and variability were both overestimated. In the sensitivity experiment E10, the average and standard deviation (-14.9‰ and 1.8‰ respectively for monsoon season) were comparable with the observation (-15.2‰ and 1.8‰), and the correlation was slightly improved. Although this does not fully explain the discrepancy, it implies that the parameter controlling the equilibrium fraction ε can be problematic. The positive points are that the $\delta^{18}O_v$ and precipitation averaged over previous days showed a strong correlation ($R < 0.6$) southwest of Niamey as in the observation (Fig. S3 in Tremoy et al., 2012), which means that the relation between convective activity and the $\delta^{18}O_v$ is well represented, and that the comparable time evolution at the monthly scale (thick lines in Fig. 3). The seasonal differences were similar, suggesting that SCIAMACHY may overestimate the seasonal variability.

3.2. Evaluation of IsoGSM at the interannual scale

Finally we evaluate the reproducibility of IsoGSM at the interannual scale. Although our target is the isotope ratio of near-surface water vapor, we use the isotope ratio of precipitation to validate the model reproducibility of surface vapor isotope at the interannual timescale. The reason is twofold; one is the lack of observations of vapor isotope covering several years. The other one is the fact that the isotopic composition of the precipitation is strongly constrained by that of the local lower tropospheric vapor (Risi et al., 2008a). Hence the precipitation isotope somewhat represents surface vapor isotope, and can be used to evaluate the reproducibility of vapor isotope, even though they are not identical.

Figure 4 compares the modeled and observed time series of annual mean $\delta^{18}O_P$ at Niamey. Note that there are missing observations from 2000 to 2008, and after 2010. The correlation between them is 0.74 ($P < 0.05$). The simulated (observed) annual average is –4.6‰ (–4.1‰) and standard deviation is 1.2‰ (1.1‰). The factors controlling the variability will be discussed in Sect. 4.

3.3. Overview of IsoGSM evaluation

To summarize the evaluation results, the spatial pattern in the mean state, and the seasonal pattern driven by the Hadley circulation, monsoon flow, and convective activity are qualitatively well simulated with an emphasis on reproducibility of the interannual variability. When compared with SCIAMACHY measurements of δD, there is a slight bias in the mean state, and IsoGSM largely underestimates the seasonal δD variations. When compared with the in situ measurements, the bias and variation difference are not as large as when compared with SCIAMACHY. Although the results of the simulation in the monsoon season are not as good as those of the dry season at the daily scale, IsoGSM captures the monthly scale variability fairly well. These results suggest that the model is applicable to study the interannual variability of $\delta^{18}O$ during the monsoon season.

4. Simulated interannual variability of vapor isotope

4.1. General features of interannual variability

In this section, we explore the interannual variability of $\delta^{18}O_v$ over Niamey by the standard experiment. The simulation period is from 1979 to 2012. The most striking feature of the interannual variability is that the depletion in the monsoon season does not appear every year in the model (Fig. 4 and Fig. 5). In contrast, $\delta^{18}O_v$ depletion occurs each winter. We term the years with isotopic depletion in the monsoon season the "W-shape year" following Tremoy et al. (2012). To understand the factors controlling the interannual variability of $\delta^{18}O_v$, it is necessary to investigate the differences between the years with and without depletion. For the purpose of comparison, we set the criteria and made two composite fields: W-shape year composite and non-W-shape (NW-shape) year composite. The quantitative definition of a W-shape year is a year in which the surface vapor isotope value averaged over JAS in Niamey is 1σ (1.1‰) less than that of the climatological average (–12.9‰). We picked out six W-shape years (1988, 1999, 2009, 2010, 2011, and 2012) in the period, and the rest are appointed to the NW-shape composite. The seasonal variations in surface $\delta^{18}O_v$ in the two composite fields are shown in Fig. 5.

Here, we briefly discuss the features of the W-shape years. Figures 6 and 7 show the two composite fields and their differences (W-shape years minus NW-shape years) in the monsoon season. W-shape years are characterized by enhanced monsoon activity; the velocities of southwesterly winds over West Africa are higher (Fig. 6l), and latitudes south of 10°N receive a larger amount of precipitation, especially on the Guinean coast and the West and East Sahel (Fig. 6f). Due to the larger amount of precipitation, the level of evapotranspiration is also higher (Fig. 6i), and hence wetter conditions prevail (Fig. 6c) in W-shape years. The $\delta^{18}O_v$ is more depleted, as expected, centering on Niamey (Fig. 7c). The isotopic compositions of precipitation and evapotranspiration are also more depleted south of Niamey (Fig. 7f, i).

4.2. Factors controlling $\delta^{18}O_v$ at interannual timescales

To identify the mechanism responsible for the difference in isotopic variability between W shape and NW shape years, isoflux analysis was applied to both composite fields. Here we analyze precipitable water instead of surface vapor for two reasons: first is for the sake of simplicity. By analyzing precipitable water, we do not have to consider at what height condensation and re-evaporation take place, or the effect of vertical advection; and second, most of the atmospheric water resides near the surface, and therefore the isotopic composition of precipitable water should be useful as a proxy for surface $\delta^{18}O_v$. This kind of alternation is also seen is Tremoy et al. (2012). As the analysis specifies the contribution of each factor to the change in isotopic composition of precipitable water, the analysis period should start before the initiation of isotopic depletion and end at the most depleted point. Since the seasonal variation in the isotopic composition of precipitable water is almost the same as the surface $\delta^{18}O_v$ (Fig. 5), the analysis period was June-August to capture the decrease in isotopic composition of precipitable water.

Figure 8 shows the results for the two composite fields at the Niamey gridcell. First, we discuss how each factor contributes to the δ_W variation in general. Precipitation lowers δ_W, which is reasonable when considering the Rayleigh distillation model. That is, δ_P is greater than δ_W; therefore, the effect of precipitation is always negative, and contributes to lowering δ_W. Evapotranspiration works in the opposite way. As the model does not take fractionation into account on the land surface, δ_E can be assumed to be a mixture of all precipitation (Yoshimura et al., 2008). Hence, δ_E is presumably larger than δ_W by the same analogy used to explain the effect of precipitation, and contributes to the increase in δ_W. The impact of advection in this form in Eq. (4) seems weaker compared with the other terms. However, the impact is the temporally averaged value. Given that the advection sometimes lowers the δ_W and sometimes enriches δ_W, the fact that the averaged value is very low does not readily imply that the impact itself is small. Therefore we further decompose the effect of advection in Eq. (4) into:

$$\nabla \delta_W \cdot Q = \frac{\partial \delta_W}{\partial y} Q_N + \frac{\partial \delta_W}{\partial y} Q_S + \frac{\partial \delta_W}{\partial x} Q_E + \frac{\partial \delta_W}{\partial x} Q_W \qquad (5)$$

where Q_N, Q_S, Q_E, and Q_W, represent the vertically integrated two-dimensional vapor flux vector from the north, south, east, and west, respectively. In this form, the impact of advection becomes clearer (Fig. 8b); southerly flow decreases δ_W, and easterly flow increases δ_W. The precipitation area in the south of Niamey which produces isotopically light moisture is considered to contribute decreases δ_W. While there is relatively less precipitated area in the east of Niamey, which should produce isotopically heavier moisture compared with the southern part, contributing to increase δ_W (Fig. 6). The impacts of the westerly flow and northerly flow are ambiguous and negligible.

The $(d\delta_W/dt)W$ is low in W-shape years ($P < 0.05$). Precipitation further lowers δ_W and evapotranspiration further increases δ_W in W-shape years reflecting the larger amounts of precipitation and evapotranspiration. Although the differences between the impacts of the two composite fields are large, they are not significant because of the high degree of variation. The only term significantly different at 5% significance level other than $(d\delta_W/dt)W$ is the impact of the southerly flow. When regressed with JAS averaged surface $\delta^{18}O_v$ at the interannual timescale, the term that shows a strong correlation ($P < 0.05$) is the southerly flow alone. This suggests that the monsoon flow brings depleted moisture produced by heavier precipitation to the Niamey area, controlling the interannual variability of $\delta^{18}O_v$. The interannual regression field of JAS averaged precipitation against Niamey surface $\delta^{18}O_v$ shows the correlation at the Guinea Coast (10°W – 10°E, EQ – 10°N; Fig. 9). This indicates the relative importance of the distillation process during transport, as compared to local precipitation for the interannual variability of $\delta^{18}O_v$ in West Africa.

In this regard, the correlation between $\delta^{18}O_v$ and precipitation east of Niamey, which is also located in the upstream region of Niamey, is expected to be strong, because heavier precipitation falls in the East Sahel in W-shape years and the African Easterly Jet (AEJ) flows toward the Niamey region at heights above 800 hPa. The correlation for this region east of Niamey, however, is relatively weak ($|R| < 0.4$). As the southerly flow is dominant in the lower atmosphere (1000 – 800 hPa) in the monsoon season, the relatively weak connection between surface $\delta^{18}O_v$ and precipitation east of Niamey is reasonable.

4.3. Sensitivity experiment

To confirm the contributions of the amount of precipitation that falls at the Guinea Coast to the interannual variability in $\delta^{18}O_v$ at Niamey, we carried out the sensitivity experiment, NoFrac, in which we removed the influence of the distillation process in the Guinea Coast (10°W – 10°E, EQ – 10°N). As shown in Fig. 4, most of the interannual variability in $\delta^{18}O_v$ at Niamey was removed. In the standard experiment, the average $\delta^{18}O_v$ and the variance at

Niamey are –12.9‰ and 1.16, respectively, whereas they are –11.7‰ and 0.15, respectively, in NoFrac. The enriched average and considerably smaller variance in NoFrac confirm the key role of the Guinea Coast precipitation in controlling the interannual variability of $\delta^{18}O_v$ at Niamey. In addition, we conducted other sensitivity experiments that were the same as the sensitivity experiment NoFrac but for East Sahel (10°E – 30°E, 10°N – 20°N) and Niamey (10°E – 14°E, 11°N – 15°N). Neither of these experiments showed a significant difference from the standard experiment (data not shown): the average and variance were –12.8‰ (–12.8‰) and 1.07 (1.15), respectively, for East Sahel (Niamey). These results exclude the impact of precipitation in East Sahel or Niamey in controlling the interannual variability, and enhance the robustness of our hypothesis.

5. Relationship with ENSO

West African rainfall in the monsoon season has been connected to ENSO (e.g., Janicot et al., 2001; Joly et al., 2007; Losada et al., 2012); i.e., less precipitation during El Niño and more precipitation during La Niña. Given this connection, a relation between $\delta^{18}O_v$ and ENSO through precipitation change is expected. Indeed, three of six W-shape years (1988, 1999, and 2010) fell during a La Niña period. Therefore, we regressed JAS $\delta^{18}O_v$ from the model and annually averaged the NINO3 index calculated from the NCEP SST analysis, which was used to force the model. High positive correlations were found in all of West Africa (Fig. 10a). The spatial distribution of the correlation between the annual average of $\delta^{18}O_p$ weighted by monthly precipitation, and the annual averaged NINO3 index was almost identical to the former, but the correlated area over West Africa was confined to south of 15°N (Fig. 10b). To validate this relation, we also show the relation between observed $\delta^{18}O_p$ from GNIP and the NINO3 index. The correlation pattern agreed well with GNIP over most of Africa; the highest positive correlation was in West Africa, a weak negative correlation was seen in the south of Central and East Africa, and a weak positive correlation was found in South Africa (Fig. 10c). All of the figures indicate that $\delta^{18}O$ is significantly lower (higher) during the cold (warm) phase of ENSO over West Africa. The relation between $\delta^{18}O$ in West Africa and ENSO is evident from the figures. The relation results from the relation between $\delta^{18}O$ and West African precipitation, as discussed in Sect. 4, and between the precipitation and ENSO. This mechanism is also found in the Asian and South American monsoon regions: ENSO governs precipitation and the precipitation determines the interannual variability of the isotopic composition over the downstream regions (Vuille and Werner, 2005; Ishizaki et al., 2012).

ENSO is not the only mode affecting West African rainfall (Janicot et al., 2001); Global

Warming, inter-decadal Pacific Oscillation (IPO), and Atlantic Multidecadal Oscillation (AMO) are found to have significant impact (Mohino et al., 2011a) as well. Therefore, a non-stationary relation between West African rainfall and ENSO (Janicot et al., 1996; Losada et al. 2012) has been reported, but this lies beyond the scope of the present study. Here, we wish to emphasize that we confirmed the statistical relation between rainfall at the Guinea Coast and ENSO, in both observations (Global Precipitation Climatology Project: GPCP (Huffman et al., 2009)) ($R = -0.43$, $P < 0.05$) and the model ($R = -0.45$, $P < 0.05$) during the period 1979 – 2012. Losada et al. (2012) also showed that this relation became significant after the 1970s. Hence, we ensured the robustness of the relation between the isotope ratio in surface vapor, precipitation, and ENSO over West Africa.

6. Conclusion and perspective

Here, we presented the interannual variability of $\delta^{18}O_v$ in West Africa and its relation to ENSO using the nudged IsoGSM model (Yoshimura et al., 2008). Our simulation indicated that the isotopic depletion in the monsoon season, which was reported by Risi et al. (2010) and Tremoy et al. (2012), does not occur every year. The main driver of the depletion was found to be precipitation at the Guinea Coast. Second, we found a relation between $\delta^{18}O$ over West Africa and ENSO; ENSO modulates the interannual variability of $\delta^{18}O$ via precipitation at the Guinea Coast.

We showed the ability of the model to simulate intraseasonal to interannual time scale variability, but the model performed relatively poorly on the daily scale. The parameter controlling the equilibrium fraction ε is suggested to be problematic. Another possibility is the lack of isotopic fractionation over the land surface. Risi et al. (2013) demonstrated the importance of continental recycling and sensitivity to model parameters that modulate evapotranspiration over West Africa. They indicated the importance of taking land surface fractionation into account. As IsoGSM assumes that isotopic fractionation does not occur over the land surface, coupling with more sophisticated land surface models would allow more accurate simulations. Similarly, an atmosphere–ocean-coupled model with stable isotopes is desirable to determine how ENSO impacts isotope ratio above water more clearly.

One of the expected roles of isotope-enabled GCMs is to find “hot spots”; i.e., places at which a climate proxy is sensitive to climate change, for climate reconstruction. Here, we propose that $\delta^{18}O$ at Niamey may be a good proxy of West African rainfall and its relation to ENSO. Indeed, we found a good correlation between the simulated $\delta^{18}O$ and a climate proxy from Ghana, which has a signal of ENSO (Shanahan et al., 2009) for their overlapping period ($R = 0.65$, $P < 0.01$). Despite the strong correlation, however, ENSO is certainly not the single mode modulating $\delta^{18}O$ in the area. In our simulation, the last four years were counted as W-shape years in which surface $\delta^{18}O_v$ was lower at Niamey and precipitation over West Africa was higher, even though not all of these were La Niña years. This may reflect the recent La Niña-like trend associated with the hiatus (Kosaka and Xie, 2013; England et al., 2014), supporting the impact of Interdecadal Pacific Oscillation (IPO) on West African rainfall on a multidecadal timescale (Mohino et al., 2011a). On the other hand, Shanahan et al. (2009) reconstructed West African rainfall variability from the sediments of a lake in Ghana, supporting the suggestion that Atlantic SST controls the multidecadal variability. Further comparisons with in situ observations and climate proxies would be of interest.

This study confirms the relation between West African rainfall and isotopic variability at the interannual time scale, which enables us to reconstruct detailed West African rainfall and, this should help disentangle the non-stationarity of the impact of various SST basins on West Africa rainfall.

Acknowledgments

The first author is supported by Japan Society for the Promotion of Science (JSPS) via Grant-in-Aid for JSPS Fellows. A part of this research was supported by the SOUSEI from MEXT, Japan, CREST from JST, Japan, JSPS KAKENHI Grant Numbers 23686071, 26289160, and the GCOE for Sustainable Urban Regeneration in the University of Tokyo. R.S. acknowledges support from the Netherlands Space Office as part of the User Support Programme Space Research project GO-AO/16.

References

Aronson, R. B., Precht, W. F., Macintyre, J. G. and Murdoch, T. J. T.: Coral bleach-out in Belize, Nature, 405, 36, doi:10.1038/35011132, 2000.

Berkelhammer, M., Stott, L., Yoshimura, K., Johnson, K., and Sinha, A.: Synoptic and mesoscale controls on the isotopic composition of precipitation in the western US, Clim. Dynam., 38, 433-454, 2012.

Brown, J., Simmonds, I., and Noone, D.: Modeling $\delta^{18}O$ in tropical precipitation and the surface ocean for present-day climate, J. Geophys. Res., 111, D05105, 2006.

Cai. W., Borlace, S., Lengaigne, M., Rensch, P., Collins, M., Vecchi, G., Timmermann, A., Santoso, A., McPhaden, M. J., Wu, L., England, M. H., Wang, G., Guilyardi, E., and Jin, F.-F.: Increasing frequency of extreme El Niño events due to greenhouse warming, Nat. Clim. Chang., 4, doi:10.1038/NCLIMATE2100, 2014.

Dai, A., Fung, I. Y., Del Genio, A. D.: Surface observed global land precipitation variations during 1900-88, J. Climate, 10, 2943-2962, 1997.

Dansgaard, W., Stable isotopes in precipitation, Tellus, 16, 436-468, 1964.

England, M. H., McGregor, S., Spence, P., Meehl, G. A., Timmermann, A., Cai, W., Gupta, A., McPhaden, M. J., Purich, A., and Santoso, A.: Recent intensification of wind-driven circulation in the Pacific and the ongoing warming hiatus, Nat. Clim. Chang., 4, 222-227, 2014.

Frankenberg, C., Yoshimura, K., Warneke, T., Aben, I., Butz, A., Deutscher, N., Griffith, D., Hase, F., Notholt, J., Schneider, M., Schrijver, H., and Röckmann, T.: Dynamic processes governing lower-tropospheric HDO/H_2O ratios as observed from space and ground, Science, 325, 1374-1377, 2009.

Folland, C. K., Palmer, T. N., and Parker, D. E.: Sahel rainfall and worldwide sea temperatures, 1901-85, Nature, 320, 602-607, 1986.

Gianni, A., Saravanan, R., Chang, P.: Oceanic forcing of Sahel rainfall on interannual to interdecadal time scales, Science, 302, 1027, doi:20.1126/science.1089357, 2003.

Huffman, G. J., Alder, R. F., Bolvin, D. T., and Gu, G.: Improving the global precipitation record: GPCP Version 2.1, Geophys. Res. Lett., 36, L17808, 2009.

IAEA/WMO, Global Network of Isotopes in Precipitation, The GNIP Database, 2014. Accessible at: http://www.iaea.org/water

Ishizaki, Y., Yoshimura, K., Kanae, S., Kimoto, M., Kurita, N., and Oki, T.: Interannual variability of $H_2{}^{18}O$ in precipitation over the Asian monsoon region, J. Geophys. Res., 117, D16308, 2012.

Janicot, S., Moron, V., and Fontaine, B.: Sahel droughts and ENSO dynamics, Geophys. Res. Lett., 23 (5), 515-518, 1996.

Janicot, S., Trzaska, S., and Poccard, I.: Summer Sahel-ENSO teleconnection and decadal time scale SST variations, Clim. Dynam., 18, 303-320, 2001.

Janicot, S et al.: Large-scale overview of the summer monsoon over West Africa during the AMMA field experiment in 2006, Ann. Geophys., 26, 2569-2595, 2008.

Joly, M., Voldoire, A., Douville, H., Terray, P., and Royer, J.-F.: African monsoon teleconnections with tropical SSTs: validation and evolution in a set of IPCC4 simulations, Clim. Dynam., 29, 1-20, 2007.

Joly, M. and Voldoire, A.: Role of Gulf of Guinea in the interannual variability of the West African monsoon: what do we learn from CMIP3 coupled simulations?, Int. J. Climatol., 30, 1843-1856, 2010.

Joussaume, S., Sadourny, R., and Jouzel, J.: A general circulation model of water isotope cycles in the atmosphere, Nature, 311, 24-29, 1984.

Kanamitsu, M., Ebisuzaki, W., Woolen, J., Potter, J., and Fiorino, M.: NCEP-DOE AMIP-II Reanalysis (R-2), B. Am. Meteorol. Soc., 83, 1631-1643, 2002.

Kosaka, Y. and Xie, S.-P.: Recent global-warming hiatus tied to equatorial Pacific surface cooling, Nat. Clim. Chang., 501, 403-407, 2013.

Lai, C-T., Ehleringer, J. R., Bond, B. J., and Paw U, K. T.: Contributions of evaporation, isotopic non-steady state transpiration and atmospheric mixing on the $\delta^{18}O$ of water vapour in Pacific Northwest coniferous forests, Plant Cell Environ., 29, 77-94, 2006.

Lamb, P. J.: Large-scale tropical Atlantic surface circulation patterns associated with Subsaharan weather anomalies, Tellus, 30, 240-251, 1978.

Lee, J.-E., Risi, C., Fung, I., Worden, J., Scheepmaker, R. A., Linder, B., and Frankenberg, C.: Asian monsoon hydrometeorology from TES and SCIAMACHY water vapor isotope measurements and LMDZ simulations: Implications for speleothem climate record interpretation, J. Geophys. Res., 117, D15112, 2012.

Lézine, A.-M., and Casanova, J.: Pollen and hydrological evidence for the interpretation of past climates in tropical West Africa during the Holocene, Quaternary Science Reviews, 8, 45-55, 1989.

Liu, G., Kojima, K., Yoshimura, K., Okai, T., Suzuki, A., Oki, T., Siringan, F. P., Yoneda, M., and Kawahata, H.: A model-based test of accuracy of seawater oxygen isotope ratio record derived from a coral dual proxy method at southeastern Luzon Island, the Philippines, J. Geophys. Res-Biogeo., 118, 853-859, 2013.

Liu, Z., Yoshimura, K., Bowen, G. J., Buenning, N. H., Risi, C., Welker, J. M. and Yuan, F.: Paired oxygen isotope records reveal modern North American atmospheric dynamics during the Holocene, Nature communications, 5, 3701, doi:10.1038/ncomms4701, 2014.

Losada, T., Rodiriguez-Fonseca, B., Mohino, E., Bader, J., Janicot, S., and Mechoso, C. R.: Tropical SST and Sahel rainfall: A non-stationary relationship, Geophys. Res. Lett., 39, L12705, 2012.

Mohino, E., Janicot, S., Bader, J.: Sahel rainfall and decadal to multi-decadal sea surface temperature variability, Clim. Dynam., 37, 419-440, 2011a.

Mohino, E., Rodriguez-Fonseca, B., Losada, T., Gervois, S., Janicot, S., Bader, J., Ruti, P., and Chauvin, F.: Changes in the interannual SST-forced signals on West African rainfall. AGCM intercomparison, Clim. Dynam., 37, 1707-1725, 2011b.

Moorthi, S. and Suarez, S. J.: Relaxed Arakawa-Schubert: A parameterization of moist convection for general circulation models, Mon. Weather Rev., 120, 978-1002, 1992.

Nicholson, S. E.: The West African Sahel: A review of recent studies on the rainfall regime and its interannual variability, ISRN Meteorology, 2013, 1-32, 2013.

Onogi, K., Tsusui, J., Koide, H., Sakamoto, M., Kobayashi, S., Hatsushika, H., Matsumoto, T., Yamazaki, N., Komahori, H., Takahashi, K., Kadokura, S., Wada, K., Kato, K., Oyama, R., Ose, T., Mannoji, N., and Taira, R.: The JRA-25 Reanalysis, 85, 369-432, 2007.

Palmer, T. N.: Influence of the Atlantic, Pacific and Indian Ocean on Sahel rainfall, Nature, 322, 251-253, 1986.

Philander, S. G. H.: Anomalous El Niño of 1982-1983, Nature, 305, 16, doi:10.1038/305016a0, 1983.

Polo, I., Rodriguez-Fonseca, B., Losada, T., and Garcia-Serrano, J.: Tropical Atlantic variability modes (1979-2002). Part I: Time-evolving SST modes related to West African rainfall, J. Climate, 21, 6457-6475, 2008.

Risi, C., Bony, S., and Vimeux, F.: Influence of convective processes on the isotopic composition ($\delta^{18}O$ and δD) of precipitation and water vapor in the tropics: 2. Physical interpretation of the amount effect, J. Geophys. Res., 113, D19306, 2008a.

Risi, C., Bony, S., Vimeux, F., Descroix, L., Ibrahim, B., Lebreton, E., Mamadou, I., and Sultan, B.: What controls the isotopic composition of the African monsoon precipitation? Insights from event-based precipitation collected during the 2006 AMMA field campaign, Geophys. Res. Lett., 35, L24808, 2008b.

Risi, C., Bony, S., Vimeux, F., Frankenberg, C., Noone, D., and Worden, J.: Understanding the Sahelian water budget through the isotopic composition of water vapor and precipitation, J. Geophys. Res., 115, D24110, 2010.

Risi, C., Noone, D., Frankenberg, C., and Worden, J.: Role of continental recycling in intraseasonal variations of continental moisture as deduced from model simulations and water vapor isotopic measurements, Water Resour. Res., 49, 4136-4156, 2013.

Rowell, D. P.: The impact of Mediterranean SSTs on the Sahelian rainfall season, J. Climate, 16, 849-862, 2003.

Scheepmaker, R. A., Frankenberg, C., Deutscher, N. M., Schneider, M., Lnadgraf, J., and Aben, I.: Validation of SCIAMACHY HDO/H2O measurements using the TCCON and NDACC-MUSICA networks, Atmos. Meas. Tech. Discuss., 7, 11799-11851, 2014.

Schmidt, G. A., LeGrande, A., and Hoffmann, G.: Water isotope expressions of intrinsic and forced variability in a coupled ocean-atmosphere model, J. Geophys. Res., 112, D10103, 2007.

Shanahan, T. M., Overpeck, J. T., Anchukaitis, K. J., Beck, J. W., Cole, J. E., Dettman, D. L., Peck, J. A., Scholz, C. A., and King, J. W.: Atlantic forcing of persistent drought in West Africa, Science, 324, 377-380, 2009.

Tindall, J.C., Valdes, P. J., and Sime, L. C.: Stable water isotopes in HadCM3: Isotopic signature of El Nino-Southern Oscillation and tropical amount effect, J. Geophys. Res., 114, D04111, 2009.

Tremoy, G., Vimeux, F., Mayaki, S., Souley, I., Cattani, O., Risi, C., Favreau, G., and Oï, M.: A 1-year long δ^{18}O record of water vapor in Niamey (Niger) reveals insightful atmospheric processes at different timescales, Geophys. Res. Lett., 39, L08805, 2012.

Tremoy, G., Vimeux, F., Soumana, S., Souley, I., Risi, C., Favreau, G., and Oï, M.: Clustering mesoscale convective systems with laser-based water vapor δ^{18}O monitoring in Niamey (Niger), J. Geophys. Res., doi: 10.1002/2013JD020968, 2014.

Vuille, M., and Werner, M.: Stable isotopes in precipitation recording South American summer monsoon and ENSO variability: observations and model results, Clim. Dynam., 25, 401-413, 2005.

Ward, N.: Diagnosis and short-lead time prediction of summer rainfall in tropical North Africa at interannual and multidecadal timescales, J. Climate, 11, 3167-3191, 1998.

Werner, M., Langebroek, P. M., Carlsen, T., Herold, M., and Lohmann, G.: Stable water isotopes in the ECHAM5 general circulation model: Toward high-resolution isotope modeling on a global scale, J. Geophys. Res., 116, D15109, 2011.

Worden J., Noone, D., and Bowmann, K.: Importance of rain evaporation and continental convection in the tropical water cycle, Nature, 445, 528-532, 2007.

Yoshimura, K., Kanamitsu, M., Noone, D., and Oki, T.: Historical isotope simulation using Reanalysis atmospheric data, J. Geophys. Res., 113, D19108, 2008.

Yoshimura, K., Frankenberg, C., Lee, J., Kanamitsu, M., Worden, J., and Röckmann, T.: Comparison of an isotopic atmospheric general circulation model with new quasi-global satellite measurements of water vapor isotopologues, J. Geophys. Res., 116, D19118, 2011.

Table Captions

Table 1. Locations and operational periods of the GNIP observatories used in this study.

Table 2. Averages, standard deviations, their differences (simulations minus observations) and correlation coefficients for the simulations and observations from the 2010 to 2011 time series. $*P < 0.05$.

Figure Captions

Figure 1. Annual mean δD (‰) in column vapor by (a) SCIAMACHY and (b) collocated IsoGSM. Regions in which the measurements did not pass the retrieval criteria were left blank. The shaded grid with dots represents the mean value of the average, which consists of at least 10 measurements within every 6h. Annual mean precipitable water (kg/m^2) by (c) JRA25 and (d) IsoGSM is also shown.

Figure 2. Time–latitude diagrams of δD (‰) in column vapor averaged over 5°W – 5°E from 2003 to 2007 by (a) SCIAMACHY and (b) collocated IsoGSM. Regions in which the measurements did not pass the retrieval criteria are left blank. The shaded grid with dots represents the mean value of the average, which consists of at least 10 measurements within every 6h. Same as in (a-b) but for precipitable water (kg/m^2) by (c) JRA25 and (d) IsoGSM

is also shown.

Figure 3. Temporal evolution from June 2010 to May 2011 of near-surface $\delta^{18}O_v$ (‰): the thin red and green lines are the daily averaged observations and model values, respectively. The thick red and green lines connected by dots are the monthly averaged observations and model values, respectively.

Figure 4. Interannual variability of annual mean $\delta^{18}O_p$ (‰) at Niamey by the standard experiment (green) and by GNIP observation (red), together with that of near-surface $\delta^{18}O_v$ (‰) during JAS at Niamey by the standard experiment (black) and the sensitivity experiment NoFrac (white).

Figure 5. Seasonal variation of surface $\delta^{18}O_v$ (‰) in W-shape years (red) and NW-shape years (black). Bars denote the interannual standard deviations for each month of the two composite fields. Closed red squares indicate that the monthly $\delta^{18}O_v$ in the W-shape year differs significantly from NW-shape year ($P < 0.05$).

Figure 6. JAS average of 2 m height specific humidity (g/kg) (a) in W-shape years, (b) in NW-shape years, and (c) the difference between them. (d – f) Same as in (a – c) but for precipitation (mm/day). (g – i) Same as in (a – c) but for evapotranspiration (mm/day). (j –

l) Same as in (a-c) but for geopotential height at 925 hPa (gpm). Vectors denote wind at 925 hPa.

Figure 7. JAS average of isotopic composition of 2 m height vapor (‰) (a) in W-shape years, (b) in NW-shape years, and (c) the difference between them. (d – f) Same as in (a – c) but for isotopic composition of precipitation (‰). (g – i) Same as in (a – c) but for $\delta^{18}O$ in evapotranspiration (‰).

Figure 8. (a) Temporal derivative of the isotopic composition in precipitable water during JJA and the contributions of advection, evapotranspiration, and precipitation to the vapor isotope change in NW-shape years (white) and W-shape years (gray) (‰ mm/day). (b) Same as in (a), but for the decomposed terms of the advection isoflux (‰ mm/day). *$P < 0.05$ between two composites.

Figure 9. Correlation coefficient between JAS averaged $\delta^{18}O_v$ at Niamey (green dot) and precipitation. The contoured area represents statistical significance ($P < 0.01$).

Figure 10. Correlation coefficient between the annual averaged NINO3 index and a) the simulated July – September averaged vapor isotope ratio, b) annual averaged simulated precipitation isotope ratio weighted by monthly precipitation, and c) annual averaged

observed precipitation isotope ratio weighted by monthly precipitation. Regions with significant positive (negative) correlations at the 90% confidence level are circled with solid (dotted) lines in a) and b). Sites with significant correlations at the 90% confidence level are indicated by crosses in c).

Tables

Table 1. Locations and operational periods of the GNIP observatories used in this study.

Station Name	Latitude	Longitude	Operation Period
Tunis	36°50’N	10°14’E	1967-2006
Algiers	36°47’N	3°03’E	1998-2006
Sfax	34°43’N	10°41’E	1992-2008
Fes Sais	33°58’N	4°59’W	1994-2008
Sidi Barrani	31°38’N	25°57’E	1978-2003
Bamako	13°42’N	8°00’W	1962-2007
Niamey	13°29’N	2°05’E	1992-2009
N'djamena	12°08’N	15°02’E	1960-1995
Addis Ababa	9°00’N	38°44’E	1961-2009
Sao Tome	0°23’N	6°43’E	1962-1976
Entebbe	0°03’N	32°27’E	1960-2006
Kinshasa	4°22’S	15°15’E	1961-1972
Diego Garcia Island	7°19’S	72°26’E	1962-2003
Dar Es Salaam	6°53’S	39°12’E	1960-1976
Ascension Island	7°55’S	14°25’W	1961-2009
Malange	9°33’S	16°22’E	1969-1983
Ndola	13°00’S	28°39’E	1968-2009
Menongue	14°40’S	17°42’E	1969-1983
St. Helena	15°58’S	5°42’E	1962-1975
Harare	17°48’S	31°01’W	1960-2003
Antananarivo	18°54’S	47°32’E	1961-1975
Saint Denis	20°54’S	55°29’E	2001-2009
Windhoek	22°57’S	17°09’E	1961-2001
Pretoria	25°43’S	28°10’E	1958-2001
Malan	33°58’S	18°36’E	1961-2009
Cape Town	33°57’S	18°28’E	1995-2008
Gough Island	40°21’S	9°53’W	1960-2009
Marion Island	46°53’S	37°52’E	1961-2009

Table 2. Averages, standard deviations, their differences (simulations minus observations) and correlation coefficients for the simulations and observations from the 2010 to 2011 time series. *P < 0.05.

		Ave. [‰]			S.D. [‰]			Cor.
		Sim.	Obs.	Diff.	Sim.	Obs.	Diff.	
Std.	whole period	-14.6	-13.7	0.9	2.2	2.1	0.1	0.46*
	monsoon season	-16.1	-15.2	0.9	2.3	1.8	0.5	0.16
	dry season	-14.7	-15.0	-0.3	1.7	1.6	0.1	0.63*
E10	whole period	-13.9		-0.2	1.7		-0.4	0.46*
	monsoon season	-14.9		-0.3	1.8		0.0	0.20
	dry season	-15.2		-0.2	1.7		0.1	0.64*

Figures

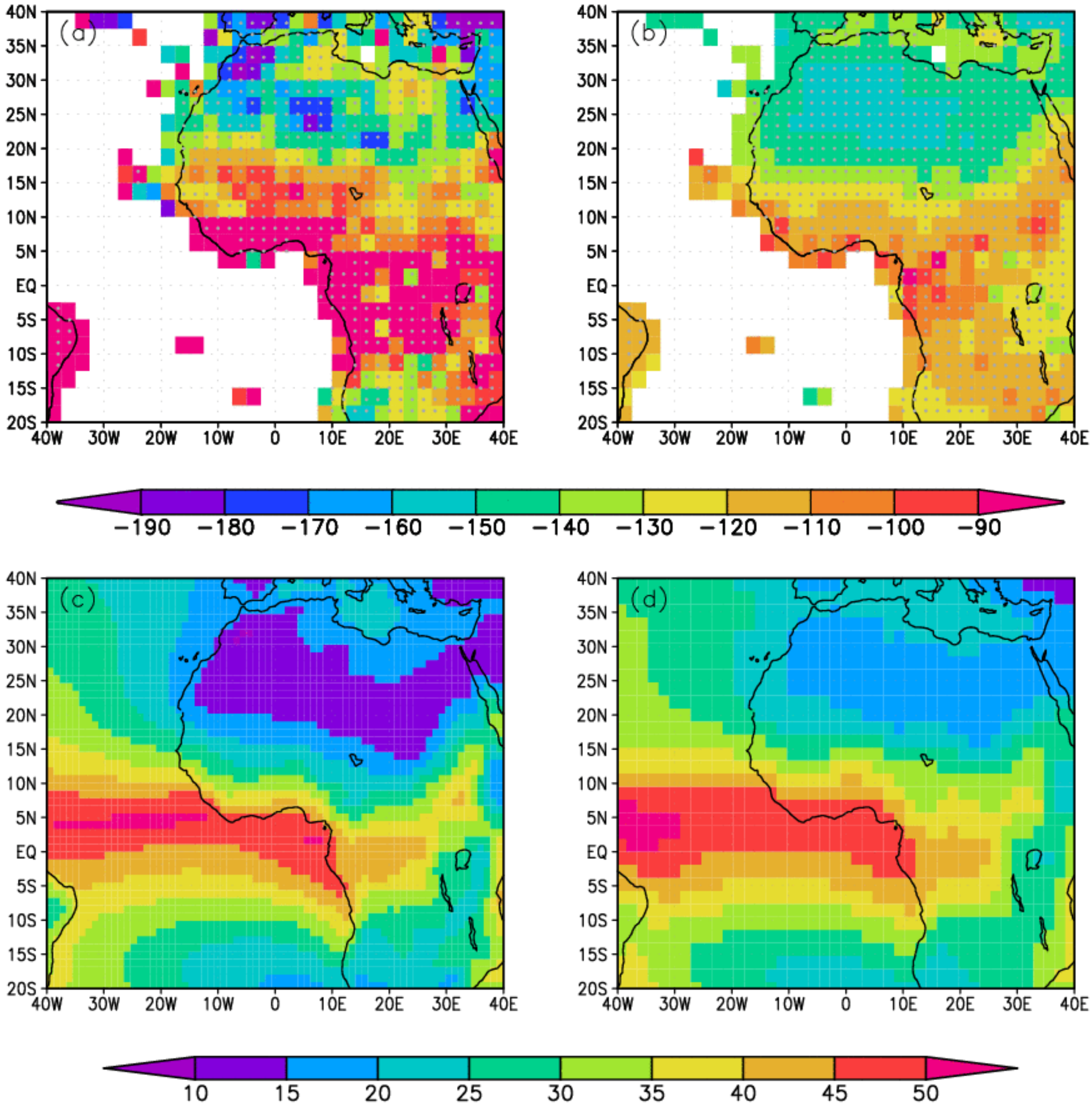

Figure 1. Annual mean δD (‰) in column vapor by (a) SCIAMACHY and (b) collocated IsoGSM. Regions in which the measurements did not pass the retrieval criteria were left blank. The shaded grid with dots represents the mean value of the average, which consists of at least 10 measurements within every 6h. Annual mean precipitable water (kg/m2) by (c) JRA25 and (d) IsoGSM is also shown.

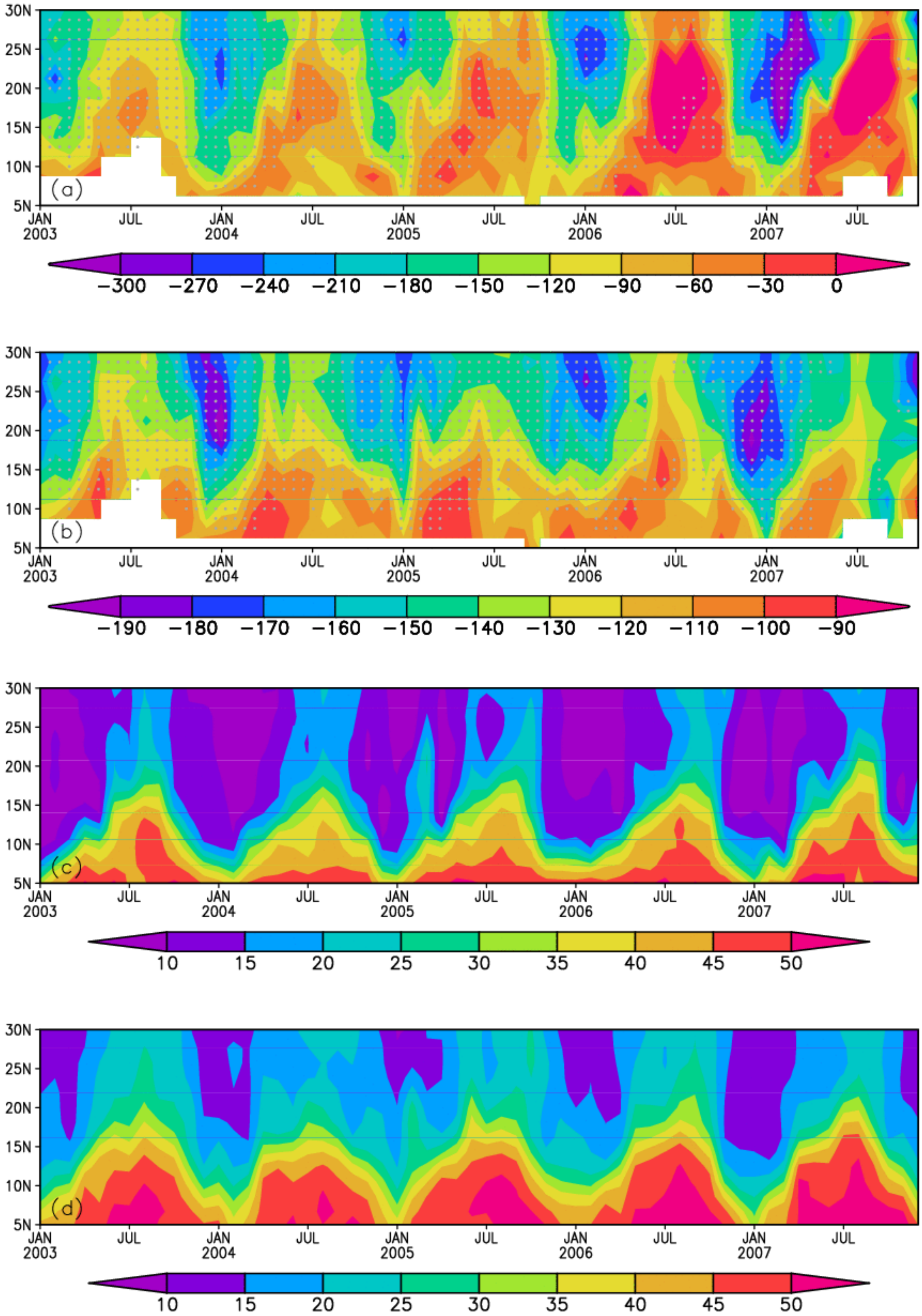

Figure 2. Time–latitude diagrams of δD (‰) in column vapor averaged over 5°W – 5°E

from 2003 to 2007 by (a) SCIAMACHY and (b) collocated IsoGSM. Regions in which the measurements did not pass the retrieval criteria are left blank. The shaded grid with dots represents the mean value of the average, which consists of at least 10 measurements within every 6h. Same as in (a-b) but for precipitable water (kg/m2) by (c) JRA25 and (d) IsoGSM is also shown.

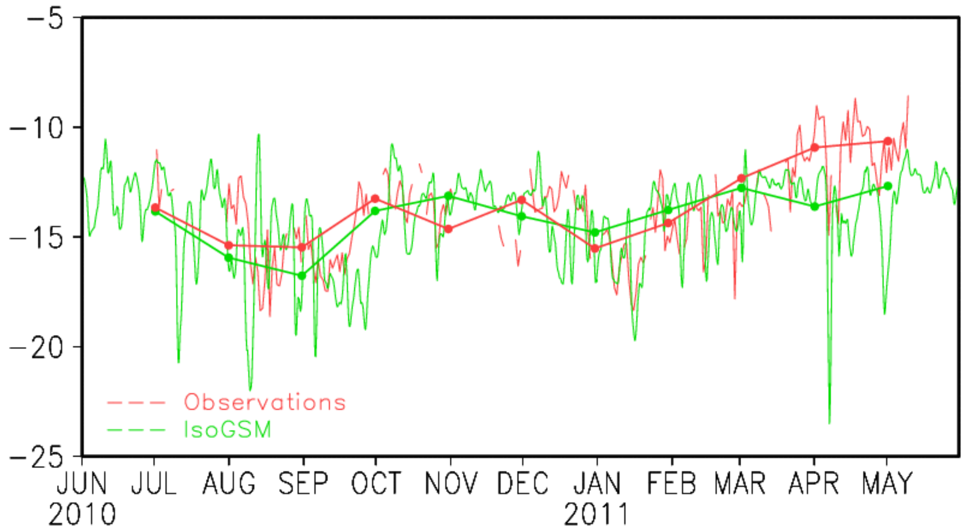

Figure 3. Temporal evolution from June 2010 to May 2011 of near-surface δ^{18}Ov (‰): the thin red and green lines are the daily averaged observations and model values, respectively. The thick red and green lines connected by dots are the monthly averaged observations and model values, respectively.

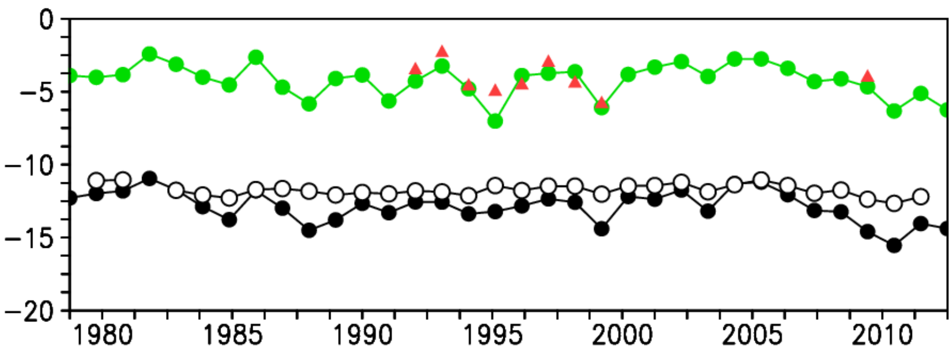

Figure 4. Interannual variability of annual mean δ^{18}Op (‰) at Niamey by the standard experiment (green) and by GNIP observation (red), together with that of near-surface δ^{18}Ov (‰) during JAS at Niamey by the standard experiment (black) and the sensitivity experiment NoFrac (white).

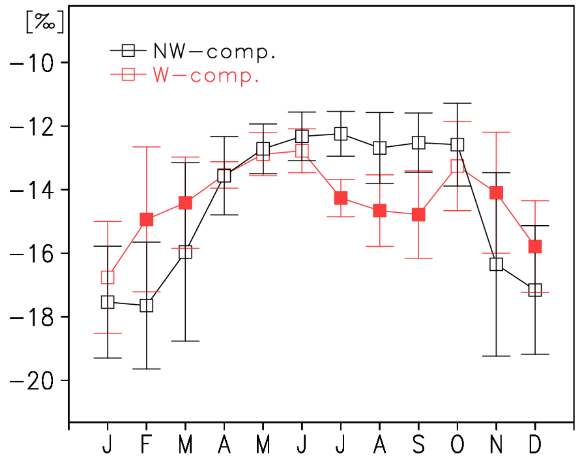

Figure 5. Seasonal variation of surface δ^{18}Ov (‰) in W-shape years (red) and NW-shape years (black). Bars denote the interannual standard deviations for each month of the two composite fields. Closed red squares indicate that the monthly δ^{18}Ov in the W-shape year differs significantly from NW-shape year ($P < 0.05$).

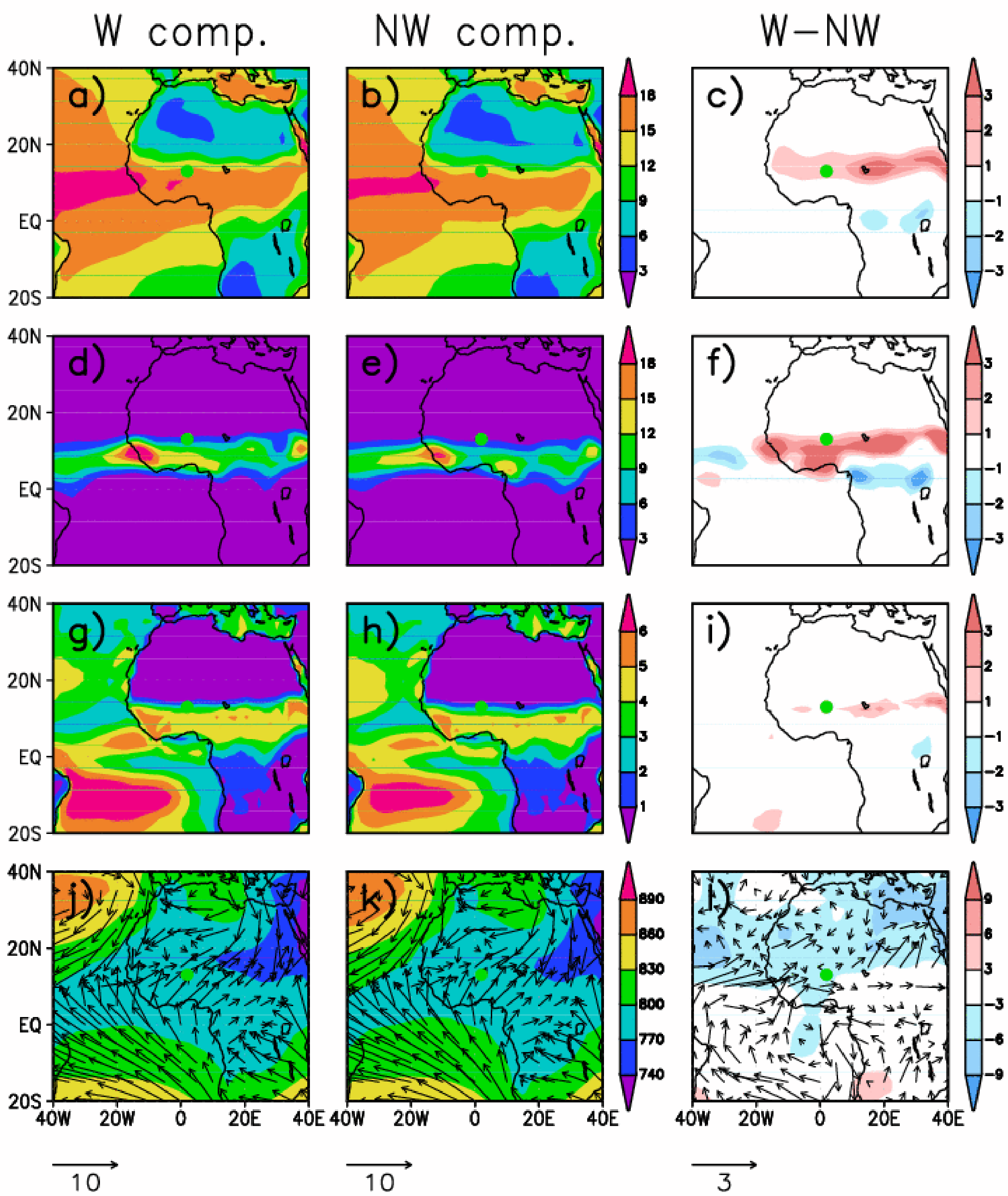

Figure 6. JAS average of 2 m height specific humidity (g/kg) (a) in W-shape years, (b) in NW-shape years, and (c) the difference between them. (d – f) Same as in (a – c) but for precipitation (mm/day). (g – i) Same as in (a – c) but for evapotranspiration (mm/day). (j – l) Same as in (a-c) but for geopotential height at 925 hPa (gpm). Vectors denote wind at 925 hPa.

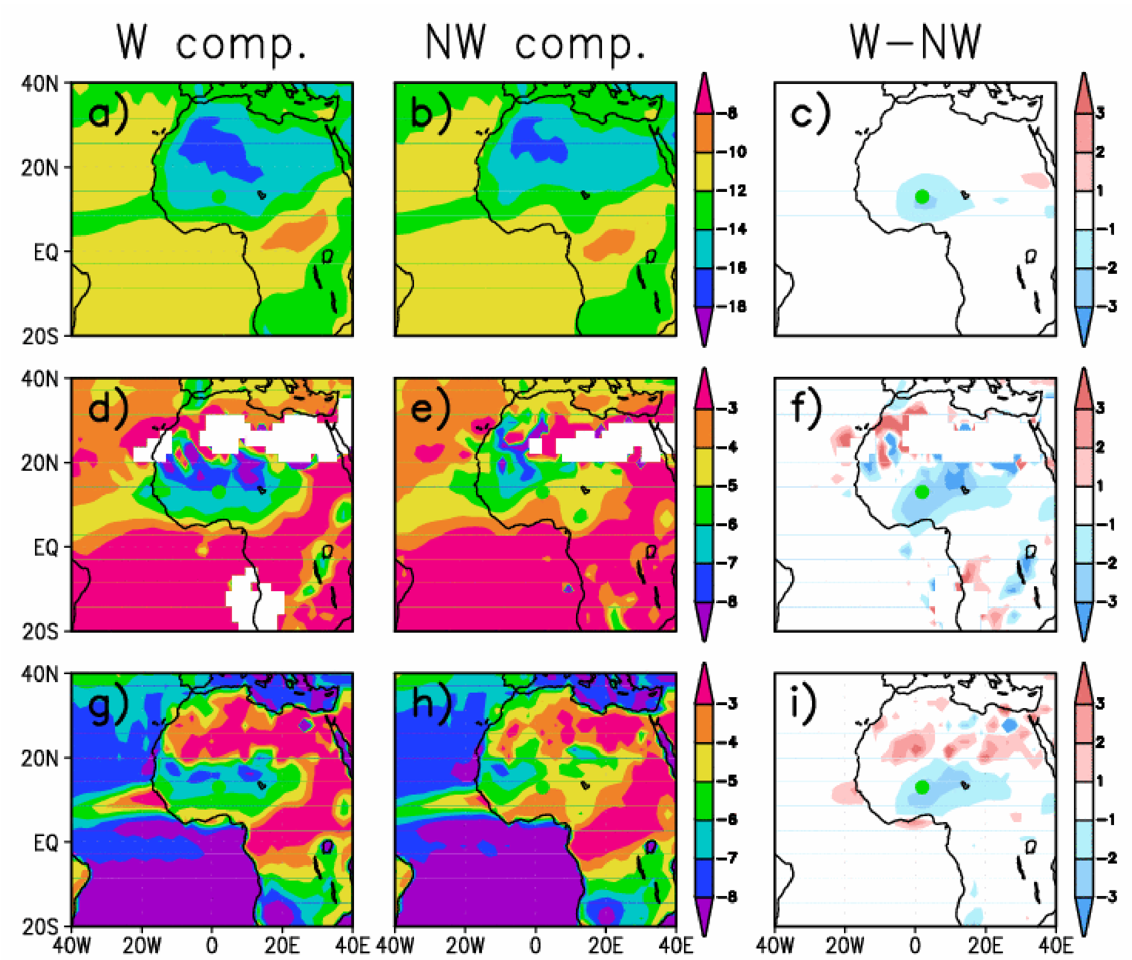

Figure 7. JAS average of isotopic composition of 2 m height vapor (‰) (a) in W-shape years, (b) in NW-shape years, and (c) the difference between them. (d – f) Same as in (a – c) but for isotopic composition of precipitation (‰). (g – i) Same as in (a – c) but for isotopic composition in evapotranspiration (‰).

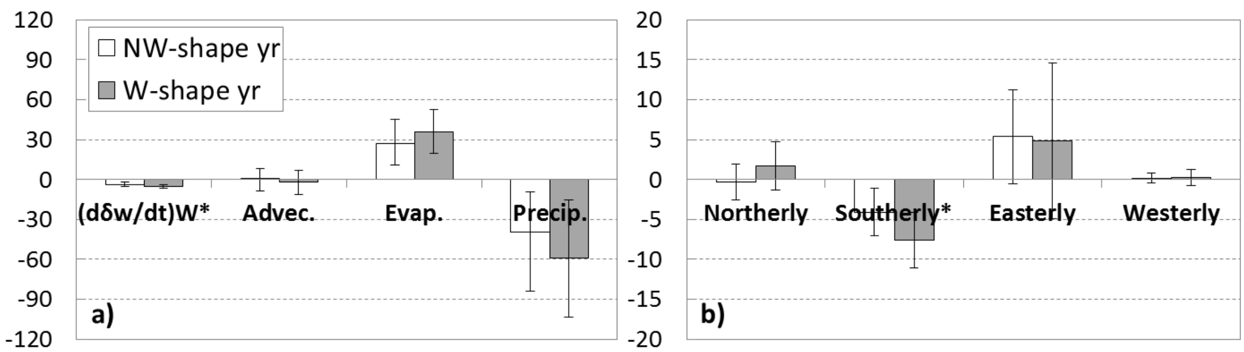

Figure 8. (a) Temporal derivative of isotopic composition in precipitable water during JJA

and the contributions of advection, evapotranspiration, and precipitation to the vapor isotope change in NW-shape years (white) and W-shape years (gray) (‰ mm/day). (b) Same as in (a), but for the decomposed terms of the advection isoflux (‰ mm/day). *P < 0.05 between two composites.

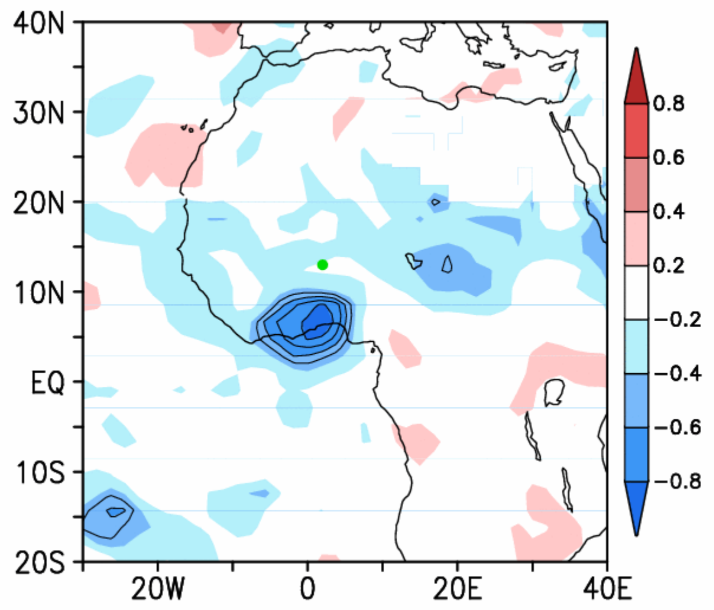

Figure 9. Correlation coefficient between JAS averaged δ^{18}Ov at Niamey (green dot) and precipitation. The contoured area represents statistical significance (P < 0.01).

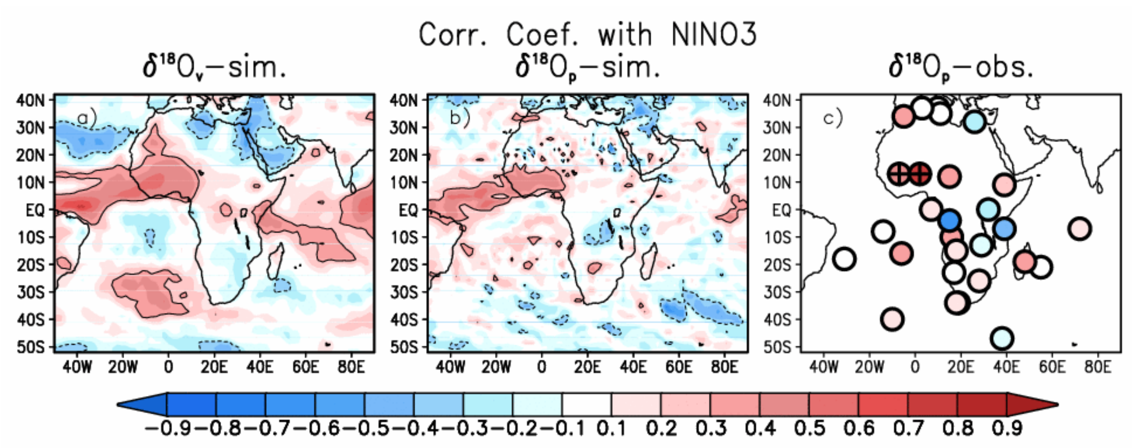

Figure 10. Correlation coefficient between annual averaged NINO3 index and a) simulated July – September averaged vapor isotope, b) annual averaged simulated precipitation isotope weighted by monthly precipitation, and c) annual averaged observed precipitation isotope weighted by monthly precipitation. Regions with significant positive (negative)

correlations at the 90% confidence level are circled with solid (dotted) lines in a) and b). Sites with significant correlations at the 90% confidence level are indicated by crosses in c).